JACS
JOURNAL OF THE AMERICAN CHEMICAL SOCIETY
Article
pubs.acs.org/JACS

Extremely Long Nonradiative Relaxation of Photoexcited Graphane Is Greatly Accelerated by Oxidation: Time-Domain Ab Initio Study

Tammie R. Nelson and Oleg V. Prezhdo*

Department of Chemistry, University of Rochester, Rochester, New York 14627, United States

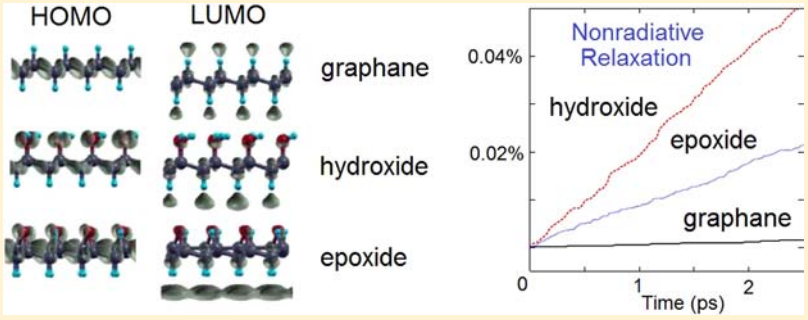

ABSTRACT: Graphane and its derivatives are stable and extremely thin, wide band gap semiconductors that promise to replace conventional semiconductors in electronics, catalysis, and energy applications, greatly reducing device size and power consumption. In order to be useful, band-gap excitations in these materials should be long lived and nonradiative energy losses to heat should be slow. We use state-of-the-art nonadiabatic molecular dynamics combined with time-dependent density functional theory in order to determine the nonradiative lifetime and radiative line width of the lowest energy singlet excitations in pure and oxidized graphanes. We predict that pure graphane has a very long nonradiative decay time, on the order of 100 ns, while epoxy- and hydroxy-graphanes lose electronic excitation energy to heat 10−20 times faster. The luminescence line width is 1.5 times larger in pristine graphane compared to its oxidized forms, and at room temperature, it is on the order of 50 meV. Hydroxylation lowers graphane's band gap, while epoxidation increases the gap. The nonradiative decay and luminescence line width of pure graphane are governed by electron coupling to the 1200 cm^{-1} vibrational mode. In the oxidized forms of graphane, the electronic excitations couple to a broad range of vibrational modes, rationalizing the more rapid nonradiative decay in these systems. The slow electron−phonon energy losses in graphane compared to other graphene derivatives, such as carbon nanotubes and nanoribbons, indicate that graphanes are excellent candidates for semiconductor applications.

1. INTRODUCTION

Graphane is a two-dimensional fully hydrogenated, sp^3-hybridized derivative of graphene produced by addition of atomic hydrogen to each site in a hexagonal graphene lattice on alternating sides of a single sheet. Theoretical prediction of this novel material[1] preceded its experimental synthesis[2] by almost 2 years, and initial electronic structure calculations found graphane to be a semiconductor with a relatively wide energy gap.[1,3] Significant effort has gone into characterization of this new and interesting material. The structural and electronic properties of graphane sheets, ribbons, and tubes[4−10] are of particular interest for incorporation into nanodevices.[11−21] The unusual properties of defect graphane structures are explored as well.[22−25] Graphene, a two-dimensional structure with extraordinary electron mobility, has proven to be an ideal material for application in modern electronics.[26] Graphane offers an effective route to expand the list of potential applications through increased semiconducting behavior while still retaining the valued reduced dimensionality of graphene. Previous studies have indicated that the electronic properties of graphene can be altered and fine tuned by chemical functionalization, particularly from oxidation.[17,27−32] Recent studies investigating hydroxylated graphane have shown that chemical functionalization also causes significant changes in the electronic properties of graphane.[6,8,33]

Electron−phonon dynamics is of fundamental importance in advancing the understanding of electronic properties in condensed phase nanoscale systems. Electron−vibrational interactions cause heating and energy loss in nanoelectronics and photovoltaics, determine the response time in conductance switches, result in coherence loss in spintronics, are responsible for charge scattering in molecular transport junctions, and constitute the most common mechanism of electron pairing in superconductors. Graphane and its derivatives constitute promising materials for these and related applications.[11−21] Elastic electron−vibrational scattering determines spectral line widths observed in luminescence spectroscopy. Investigation of the line widths of carbon nanotubes (CNTs) have shown that the shape dependence is distinct for ideal and doped systems and that defect species produce uniquely identifiable line widths.[34,35] Graphanes require similar studies.

Received: January 2, 2013
Published: February 1, 2013

   dx.doi.org/10.1021/ja400033g | J. Am. Chem. Soc. 2013, 135, 3702−3710

The present work investigates electron−vibrational relaxation and phonon-induced pure dephasing of the lowest energy singlet excitation in ideal graphane and graphane oxides at ambient temperature. The nonradiative energy losses are predicted to be extremely slow in graphane compared to other graphene derivatives, such as CNTs and graphene nanoribbons (GNRs), highlighting graphane as a promising competitor in the semiconductor industry. By speeding up the relaxation, graphane oxidation is analogous to creation of defects in GNRs[36] and CNTs.[37] The slow nonradiative decay in graphane is rationalized by weak nonadiabatic (NA) electron−phonon coupling, large band gap, and rapid phonon-induced loss of coherence in the electronic subsystem. The relaxation in both graphane hydroxide and epoxide is more than an order of magnitude faster due to increased NA coupling, even though the excitation energy is 1 eV larger in graphane epoxide than graphane. The homogeneous luminescence line width is around 50 meV in pristine graphane at ambient temperature. It is 1.5 times smaller in graphane epoxide and hydroxide. Hydroxylation lowers graphane's band gap, while epoxidation increases the gap. The electronic subsystem of pure graphane couples exclusively to the 1200 cm^{-1} vibrational mode, while the oxidized forms of graphane exhibit coupling to a broad range of modes, rationalizing the more rapid nonradiative energy losses.

The study employs the state-of-the-art approach[37−40] detailed in the next section. The technique combines time-dependent density functional theory (TDDFT)[41] with NA molecular dynamics (MD).[42−44] The Results and Discussion section includes a description of the graphane systems used in our calculations and a detailed analysis of the electron−phonon interaction, nonradiative relaxation, pure dephasing, and luminescence line widths of the lowest energy singlet excitation in graphane and its hydroxide and epoxide.

2. COMPUTATIONAL METHODOLOGY

The dynamics simulations performed here employ a mixed quantum-classical framework in which the lighter electronic degrees of freedom are treated quantum mechanically, while the much heavier atomic cores are described classically. The classical approximation for the nuclear motions is critical, since it provides dramatic computational savings. Coupling the dynamics of quantum and classical subsystems is not a trivial task.[45−47] The quantum degrees of freedom evolve under the influence of the classical subsystem, which enters the quantum Hamiltonian as a classical external field. Semiclassical corrections arising from the collective quantum mechanical properties of the nuclear motions may be needed and are made, as described below.[37,45,48] The motion of the classical subsystem should properly correlate with the more complex quantum dynamics. In a fully quantum description, the wave function describing the atomic motion splits into branches which overlap and interfere. Surface hopping (SH) is a quantum-classical approach that incorporates branching.[42] It uses a stochastic algorithm that can be viewed as a quantum master equation. SH satisfies approximately the detailed balance between the electronic transitions upward and downward in energy and ensures that transitions up in energy are less likely than transitions down in energy by the Boltzmann factor.[43] This feature is essential for studying electron−vibrational relaxation and achieving thermodynamic equilibrium in the long time limit. The semiclassical correction to the quantum−classical SH approach represents the divergence of the parts of the nuclear wave function associated with different electronic states and incorporates the resulting loss of coherence within the electronic subsystem.[37,48]

2.1. Phonon-Induced Pure Dephasing and Optical Line Width. Optical line widths arise from both homogeneous and inhomogeneous broadening. Homogeneous broadening is induced by electron−vibrational coupling that creates fluctuations in the electronic excitation energy. While homogeneous broadening occurs at the single-molecule level, inhomogeneous broadening is an ensemble property. It is related to variations in the local environment surrounding the chromophore. In the absence of inhomogeneous broadening, the line width, Γ, is determined by the pure-dephasing time, T_2^*, and the excited-state lifetime, T_1

$$\Gamma = \frac{1}{T_2} = \frac{1}{T_1} + \frac{1}{T_2^*} \tag{1}$$

In the above expression, T_2 represents the overall dephasing time. For cases in which the excited-state lifetime, T_1, is much longer than the pure-dephasing time, T_2^*, the contribution from T_1 is negligible and the line width is determined by T_2^* alone. The pure-dephasing time corresponds to the decoherence time that determines how long the two electronic states involved in an optical excitation exist in a quantum mechanical superposition. According to the standard interpretation of quantum mechanics, at times longer than the decoherence time, the electronic subsystem either has made the transition or remains in the initial state.

The fluctuations ΔE in the electronic excitation energy E caused by atomic motions are characterized by the energy autocorrelation function (ACF)

$$C(t) = \langle \Delta E(t) \Delta E(0) \rangle_T \tag{2}$$

Here, the brackets indicate thermal averaging over a canonical ensemble. The ACF is often normalized

$$C_{\mathrm{norm}}(t) = \frac{\langle \Delta E(t) \Delta E(0) \rangle_T}{\langle \Delta E^2(0) \rangle_T} \tag{3}$$

by its initial value $C(0) = \langle \Delta E^2(0) \rangle_T$. The square root of this value gives the average fluctuation of the excitation energy. The time scale of the ACF decay characterizes the randomness of the vibrational motions coupled to the electronic transition. A broader range of modes and larger anharmonicity induce faster decay. Fourier transform (FT) of the ACF produces the influence spectrum. The FT frequencies identify the vibrational modes that are coupled to the electronic transition, while the FT intensity shows the strength of the electron−vibrational coupling for the mode of a given frequency.

The pure-dephasing function can be computed using the second-order cumulant expansion to the optical response function[49]

$$D_{\mathrm{cum}}(t) = \mathrm{e}^{-g(t)} \tag{4}$$

where

$$g(t) = \int_0^t \mathrm{d}\tau_1 \int_0^{\tau_1} C(\tau_2)\mathrm{d}\tau_2 \tag{5}$$

Typically for condensed phase systems, the pure-dephasing function decays and converges rapidly and the cumulant approximation provides an accurate description.[35,50,51] Fast convergence is important for ab initio simulations, which are usually limited to picoseconds.

Optical line-broadening mechanisms can produce both Gaussian and Lorentzian line shapes in condensed phase systems.[49,52] In time domain, the broadening is manifested as Gaussian and exponential components, respectively. Hence, we fitted the pure-dephasing functions by a combination of a Gaussian and an exponent[35,50]

$$f(t) = \left[B \exp\left(-\frac{t}{\tau_e} \right) + (1 - B) \exp\left(-\frac{1}{2} \left(\frac{t}{\tau_g} \right)^2 \right) \right] \frac{1 + A \cos(\omega t)}{1 + A} \tag{6}$$

The normalized cosine term was added to account for oscillations that were particularly strong for the ideal graphane. In the above expression B represents the magnitude of the exponential decay component, while $1-B$ gives the magnitude of the Gaussian component. The oscillation of the dephasing function is described by the amplitude, A, and frequency, ω. The latter corresponds to the vibrational modes observed in the influence spectrum.

dx.doi.org/10.1021/ja400033g | J. Am. Chem. Soc. 2013, 135, 3702−3710

The pure-dephasing time

$$T_2^* = B\tau_e + (1 - B)\tau_g \tag{7}$$

is taken to be the weighted average of the exponential, τ_e, and Gaussian, τ_g, components in the fit eq 6 of the pure-dephasing function. In the presence of the strong oscillation in the pure-dephasing function observed for ideal graphane, the dephasing time computed using the above procedure reflects the decay envelope. If one were to fit the first 10−15 fs of the dephasing function for ideal graphane, one would estimate faster pure dephasing. In agreement with the quantum Zeno effect,[53,54] this would lead to an even longer excited-state lifetime, supporting the main conclusion of this work.

2.2. Time-Domain Density Functional Theory. Time-domain density functional theory (TDDFT)[41] expresses the electron density using the Kohn−Sham (KS) representation as

$$\rho(\mathbf{r}, t) = \sum_{p=1}^{N_e} |\phi_p(\mathbf{r}, t)|^2 \tag{8}$$

where N_e is the number of electrons and $\phi_p(\mathbf{r}, t)$ are the single-electron KS orbitals. Evolution of $\phi_p(\mathbf{r}, t)$ is determined by application of the time-dependent variational principle to the expectation value of the KS density functional. It leads to the following equations of motion for the single-particle KS orbitals

$$i\hbar\frac{\partial\phi_p(\mathbf{r}, t)}{\partial t} = H(\phi(\mathbf{r}, t))\phi_p(\mathbf{r}, t),\ p = 1, ..., N_e \tag{9}$$

The equations are coupled, since the Hamiltonian H depends on the density, eq 8, obtained by summing over all KS orbitals occupied by the N_e electrons. Expanding the time-dependent KS orbitals $\phi_p(\mathbf{r}, t)$ in the adiabatic KS orbital basis $\tilde{\phi}_k(\mathbf{r}; \mathbf{R})$

$$\phi_p(\mathbf{r}, t) = \sum_{k=1}^{N_e} c_{pk}(t)|\tilde{\phi}_k(\mathbf{r}; \mathbf{R})\rangle \tag{10}$$

transforms the TDKS eq 9 into the equation of motion for the expansion coefficients[38]

$$i\hbar\frac{\partial c_{pk}(t)}{\partial t} = \sum_{m=1}^{N_e} c_{pm}(t)(\varepsilon_m\delta_{km} + \mathbf{d}_{km}\cdot\dot{\mathbf{R}}) \tag{11}$$

The nonadiabatic (NA) coupling

$$d_{km}\cdot\dot{\mathbf{R}} = -i\hbar\langle\tilde{\phi}_k(\mathbf{r}; \mathbf{R})|\nabla_R|\tilde{\phi}_m(\mathbf{r}; \mathbf{R})\rangle\cdot\dot{\mathbf{R}} \tag{12}$$

$$= -i\hbar\left\langle \tilde{\phi}_k(\mathbf{r}; \mathbf{R})\left|\frac{\partial}{\partial t}\right|\tilde{\phi}_m(\mathbf{r}; \mathbf{R})\right\rangle \tag{13}$$

arises from the dependence of the adiabatic KS orbitals on the atomic evolution $\mathbf{R}(t)$. It is computed numerically[38,55] using eq 13.

It is important to note that in the majority of publications the term TDDFT refers to the Casida equations[56] obtained as a response theory approximation to the time-domain TDDFT eq 9 and aimed at calculating electronic excitation energies. Other studies solve the time-domain electronic eq 9 with fixed nuclear positions. The current work simulates, in time domain, electron dynamics coupled to nuclear motions. On a related note, DFT employs an effective independent particle representation and incorporates electron correlation effects arising from electron−electron interactions implicitly through the choice of a DFT functional. More advanced many-body theories, such as the GW and Bethe−Salpeter approaches constructed on top of DFT, include such effects explicitly.[19] The explicit electron−hole interactions considered in these approaches result in formation of excitons. Presently, such approaches are too computationally expensive and cannot be used to study time-domain electron−phonon dynamics in nanoscale materials at the ab initio level of description of the electronic structure.

2.3. Fewest Switches Surface Hopping. Fewest switches SH (FSSH) is an algorithm for modeling dynamics of mixed quantum−classical systems.[42,43] The algorithm was implemented within TDDFT in ref 38, applied to a number of nanoscale systems,[14,36,37,40,55,57−61] and tested in ref 39. FSSH prescribes a probability for hopping between quantum states based on the evolution of the coefficients given by eq 11. The probability of a hop between states k and m within the time interval dt is given by

$$dP_{km} = \frac{b_{km}}{a_{kk}}dt \tag{14}$$

where

$$b_{km} = -2Re(a_{km}^*\mathbf{d}_{km}\cdot\dot{\mathbf{R}});\ a_{km} = c_k c_m^* \tag{15}$$

For simplicity the first subscript p used in eq 11 for evolution of the expansion coefficients has been dropped in the above expression. The velocity rescaling and hop rejection rules in FSSH lead to detailed balance between the upward and the downward transitions.[43] The current, simplified FSSH makes the assumption that the energy exchanged between the electronic and the vibrational degrees of freedom during the hop is redistributed among all vibrations much faster than the interval between the hops. With this assumption, the distribution of energy in the vibrational modes is Boltzmann at all times and the velocity rescaling and hop rejection step can be replaced by multiplying the probability, eq 14, for transitions upward in energy by the Boltzmann factor.[55] This simplification of the original FSSH technique gives great computational savings, allowing us to determine the time-dependent potential that drives the dynamics of the electronic subsystem using a single molecular dynamics (MD) trajectory. The current simulation employs the excited-state trajectory for each system. In a more general context, the technique is often referred to as the classical path approximation.[62]

2.4. Decoherence Correction in Surface Hopping. By treating atoms classically, the original FSSH scheme[42,43] excludes coherence loss that occurs in the electronic subsystem due to coupling to quantum vibrations.[37,45,48] Decoherence can be neglected if it is slower than the quantum transition time.[55,59] In the present case, the decoherence time is identified with the pure-dephasing time, eq 7. The nonradiative decay studied here takes nanoseconds and is significantly slower than decoherence. Hence, a semiclassical decoherence correction should be used with SH.[45,48,63,64] It was implemented within the TDDFT-FSSH scheme in ref 37. In the current simulation, the TDKS wave function $\phi_p(\mathbf{r}, t)$ was collapsed to an adiabatic eigenstate $\tilde{\phi}_k(\mathbf{r}; \mathbf{R})$, eq 10, on the decoherence time scale. The collapse procedure is equivalent to resetting to zero the off-diagonal matrix elements a_{km}, eq 15, entering the surface-hopping transition rate, eq 14. Collapse times were determined by a sequence of random numbers sampled from the Poisson distribution with the characteristic time given by the pure-dephasing time. The probability of collapse onto eigenstate k was given by the square of the coefficient c_k at the collapse time.

Decoherence provides a solution to the trajectory branching problem in mixed quantum−classical simulations. In a fully quantum−mechanical description of a system comprised of electrons and nuclei, the nuclear wavepackets can split and follow alternative evolutions correlated with different electronic states. Classical trajectories of nuclei do not split and therefore cannot describe this correlation. SH techniques were designed to allow classical trajectory branching. Viewed as a stochastic measurement process, decoherence provides the physical basis for the trajectory branching and eliminates the need for ad hoc SH algorithms.[63] It has been used to formulate decoherence-induced SH[65] and related[63,66,67] algorithms.

2.5. Simulation Details. The electronic structure and adiabatic MD were computed with the Vienna Ab initio Simulation Package (VASP) code[68] using a converged plane-wave basis DFT in cubic simulation cells periodically replicated in three dimensions. The generalized gradient approximation of Perdew, Burke, and Ernzerhof[69] and projector-augmented wave pseudopotentials[70] were used. The graphane and graphane oxide sheets are naturally periodic in x and y directions. In order to avoid fictitious interactions along the z axis, 8 Å of vacuum were added between the replicated sheets. The initial structures were obtained by minimization of the total energy of each

dx.doi.org/10.1021/ja400033g | J. Am. Chem. Soc. 2013, 135, 3702−3710

system, including relaxation of both sheet geometry and simulation cell size. The systems were then brought to a temperature of 300 K by repeated velocity rescaling. Microcanonical trajectories of 5 ps were produced using the Verlet algorithm with a 1 fs time step and Hellmann–Feynman forces in the first excited electronic state. The trajectories from the microcanonical MD were then used to sample 500 initial conditions to create ensemble averages for the NA dynamics. The TDKS eqs 11 were solved using the 10^{-3} fs time step.

3. RESULTS AND DISCUSSION

3.1. Geometric and Electronic Structure of Pristine Graphane and Its Epoxide and Hydroxide. The present study focuses on three graphane systems shown in Figure 1. We use the more favorable chairlike conformation for graphane, identified by Sofo et al.,[1] with hydrogen atoms arranged on either side of the plane in an alternating "up–down" fashion. We also investigate two oxidized structures formed by functionalization with hydroxyl and epoxide groups, motivated with previous studies by Nakamura et al.[8] and Ito et al.,[30] respectively. For the epoxide, we adopt a 16.7% coverage of homogeneously arranged oxygen atoms, similar to the structure reported to produce the most stable graphene analogue.[30] To create hydroxylated graphane we replaced every second hydrogen with a hydroxyl group, corresponding to 50% coverage. The simulation cells shown in Figure 1 are replicated periodically, forming infinite two-dimensional sheets of graphane, graphane hydroxide, and graphane epoxide.

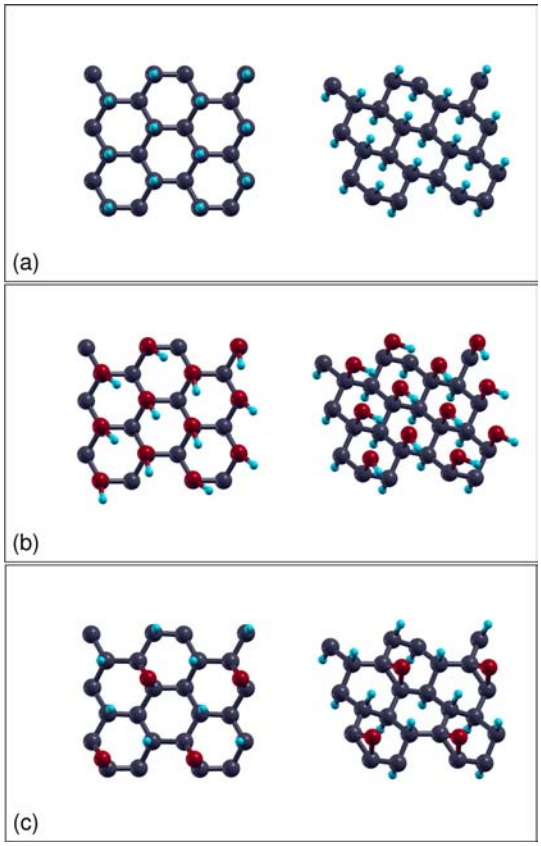

Figure 1. Top and perspective views of graphane sheets in the stable chair conformation at 300 K. (a) Ideal graphane consisting of sp^3-hybridized carbon centers and two oxidized sheets functionalized by (b) hydroxyl and (c) epoxide groups were used in the present study. Gray, blue, and red spheres represent carbon, hydrogen, and oxygen atoms, respectively.

Formation of graphane causes carbon atoms to change from sp^2 to sp^3 hybridization,[71−73] which removes the conducting π-bonding network and opens an energy gap between the valence and the conduction bands. Ideal graphane and hydroxylated graphane are semiconductors with the Γ point band gaps of 3.43 and 2.20 eV, respectively. These values are in good agreement with the previous findings.[1,8,9] The epoxidated graphane is an insulator with a band gap of 4.50 eV. The result is similar to that observed in graphene epoxide, which also exhibits a large energy gap.[30] Doping can be used to decrease the band gap of graphanes and in combination with significant electron–phonon interactions can potentially lead to high-temperature superconductivity.[18]

The orbitals contributing to the lowest energy electronic excitations in the three systems are shown in Figure 2, including both top and side views. Electronic excitation of pristine graphane promotes electron density from the bonding σ orbitals localized in the graphane plane along the carbon–carbon bonds to the antibonding σ orbitals between the carbon and the hydrogen atoms perpendicular to the plane. This is seen particularly well in the side view of the densities of the highest occupied and lowest unoccupied molecular orbitals, HOMO and LUMO, respectively. Similar types of excitation are seen for the oxidized graphanes in Figure 2b and 2c. The

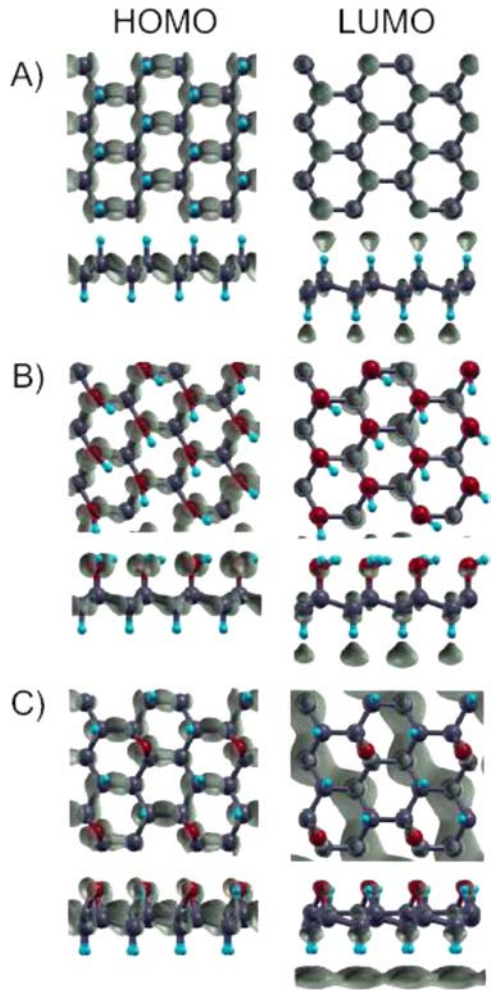

Figure 2. Densities of the highest occupied (HOMO) and lowest unoccupied (LUMO) molecular orbitals contributing to the lowest energy electronic excitations in the graphanes shown in Figure 1.

dx.doi.org/10.1021/ja400033g | J. Am. Chem. Soc. 2013, 135, 3702–3710

electron density shifts from the bonding in-plane HOMOs to the antibonding out-of-plane LUMOs. The symmetry breaking between the opposite sides of the oxidized graphanes leads to photoinduced charge transfer across the graphane layer. These DFT results show good agreement with the more advanced GW and Bethe–Salpeter calculations.[19] The electronic density in the hydroxylated graphane moves from the more electronegative oxygens of the OH groups to the less electronegative hydrogens on the opposite side of the sheet, Figure 2b. Epoxy-graphane exhibits an even stronger electron transfer from the oxygens to the hydrogens. The LUMO of epoxy-graphane is localized on top of the hydrogens and away from the sheet, forming continuous density distributions, Figure 2c.

3.2. Electron–Vibrational Interactions. Coupling to vibrational motions generates a fluctuation in the electronic energy, and generally, the extent of the fluctuation characterizes the strength of the electron–phonon coupling. Figure 3 shows

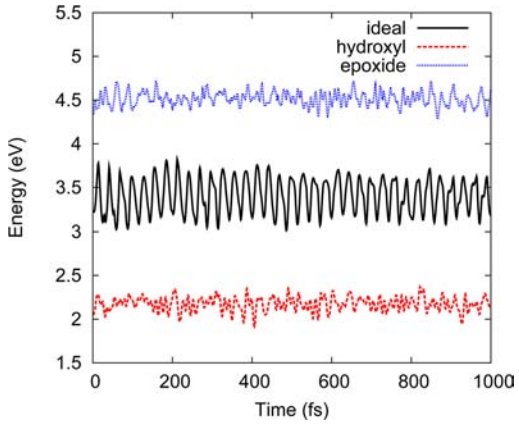

Figure 3. Fluctuations of the lowest singlet excitation energy for graphane (solid black line) and graphane oxides functionalized by hydroxyl (dashed red line) and epoxide (dotted blue line) groups at 300 K.

the evolution of the lowest electronic excited-state energy in the three systems under investigation over a 1 ps time interval. Hydroxylation lowers the excitation energy, while epoxidation increases it. The fluctuations in the excitation energy are largest in ideal graphane and appreciably reduced in the oxidized sheets. This result may appear surprising, since the hydroxyl and epoxyl groups can be regarded as impurities to ideal graphane and generally defects increase electron–phonon coupling due to a more localized nature of defect states. For instance, defects enhance the coupling in CNTs.[35,37] The situation seen with the graphanes is similar to that observed in GNR, where the energy fluctuation is notably larger for ideal systems than those containing defects.[36,50] The electronic excitation energy of pristine graphane exhibits a strong fluctuation with a well-defined frequency, Figure 3. The presence of hydroxyl and epoxyl groups drastically broadens the range of vibrational modes that couple to the electronic subsystem. The phases of individual modes are nearly random with respect to each other, and the mode contributions tend to cancel out. Further rationalization is given by the localization of the electronic transition density, Figure 2. The majority of the transition density is constrained within the main plane of pristine graphane. The oxygen atoms of hydroxide and epoxide pull a significant fraction of the electron density away from the sheet plane, reducing the coupling. The electronic excitation of oxidized graphanes is asymmetric and involves more atoms; therefore, it couples to a wider spectrum of phonon modes.

The randomness of the phonon-induced fluctuation in the electronic excitation energy is characterized by the energy autocorrelation functions (ACFs), eq 3, which are shown in Figure 4. Note that the time scales differ by an order of

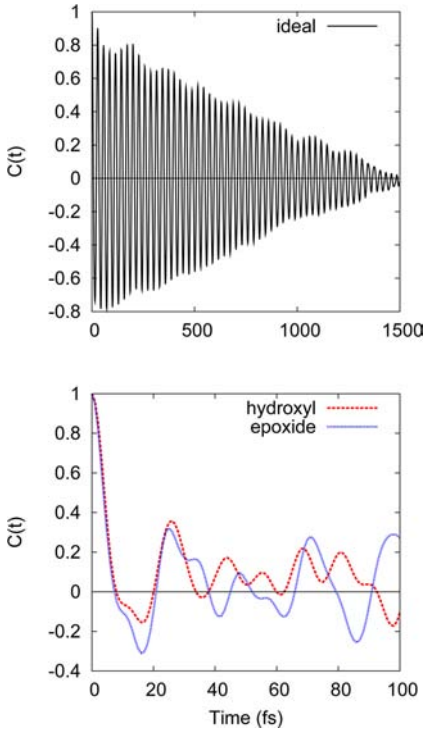

Figure 4. Normalized autocorrelation functions, eq 3, of the phonon-induced fluctuation in the lowest excitation energy of graphane (top) and graphane oxides (bottom) under investigation at 300 K. Graphane shows long vibrational coherence compared to the graphane oxides. Decay occurs on a picosecond time scale in ideal graphane and under 100 fs in the oxidized graphanes. Note the different time scales in the top and bottom panels.

magnitude in the top and bottom panels. It takes ACF more than a picosecond to decay in ideal graphane. Graphane oxidation dramatically accelerates the decay, and the ACF become asymmetric with respect to the time axis. The shorter memory in the phonon-induced fluctuation of the electronic excitation energy of graphane hydroxide and epoxide is attributed to the wider range of vibrational modes available in these systems. The less symmetric geometric structure of the oxides should make the modes less harmonic, further randomizing the energy fluctuation and accelerating the ACF decay.

Figure 5 presents the influence spectrum, computed by Fourier transforming the ACF from Figure 4. The spectrum characterizes the frequencies of the phonon modes that couple to the lowest energy electronic transition in the graphanes under study. A broad spectrum of modes interact with the electronic subsystem of the oxidized sheets. In contrast, pristine graphane couples primarily to the 1200 cm^{-1} vibration, associated with sp^3 carbon stretching.[74] Similarly, CNTs of ideal geometry couple primarily to the optical G modes near 1600 cm^{-1}, and ideal GNRs couple almost exclusively to the 1450 cm^{-1} phonon arising from the stretching mode of sp^2 carbons.[35–37,50] The intensity of the influence spectrum is an

dx.doi.org/10.1021/ja400033g | J. Am. Chem. Soc. 2013, 135, 3702–3710

Table 1. Average Excitation Energy, Nonadiabatic Coupling, Pure-Dephasing Time (T_2^*), Nonradiative Relaxation Time, and Line Width (Γ), eq 1, for Ideal and Oxidized Graphane Sheets[a]

	excitation (eV)	NA coupling (meV)	dephasing (fs)	relaxation (ns)	line width (meV)
graphane	3.43 ± 0.17	0.15 ± 0.17	13.6	160	47.7
hydroxide	2.20 ± 0.076	0.45 ± 0.33	19.1	4.8	34.5
epoxide	4.50 ± 0.080	0.65 ± 0.52	21.4	13.3	30.8

[a]The ± range bars indicate thermal fluctuation rather than error in the corresponding values.

order of magnitude larger for ideal graphane than for the oxidized graphanes, indicating that the mode at 1200 cm^{-1} couples to the electronic system more strongly than each of the multiple modes resulting from oxidation. The magnitude of the NA coupling shown in Table 1 characterizes the overall strength of the electron−phonon interaction, leading to nonradiative relaxation. Even though the electronic subsystem of ideal graphane couples to the 1200 cm^{-1} mode 10 times stronger than the oxidized graphanes to any of their modes, Figure 5, the contributions of all modes add up to create an electron−phonon interaction that is a factor of 3−4 stronger in graphane oxides than in pristine graphane.

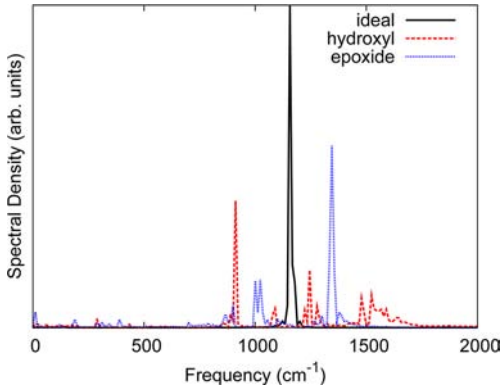

Figure 5. Influence spectra computed by Fourier transform of the ACFs shown in Figure 4. Arbitrary units used on the y axis are the same for all three systems. Data for ideal graphane have been divided by 10. Electronic excitation in ideal graphane couples exclusively to the optical phonon near 1200 cm^{-1}, while oxide excitations couple to a much wider range of vibrational motions.

3.3. Luminescence Line Width and Nonradiative Quenching. The phonon-induced pure-dephasing functions, computed according to eq 4, characterize elastic electron−phonon scattering and are shown in Figure 6. The functions were fit to eq 6 in order to obtain the pure-dephasing times. The fitting parameters are detailed in Table 2, and the dephasing times are reported in Table 1. Analysis reveals that pure dephasing occurs on a 10 fs time scale. Compared to the defects in GNRs and CNTs,[35,50] oxidation has a mild influence on the dephasing time. Graphane hydroxide and epoxide exhibit similar dephasing time scales, while ideal graphane shows slightly faster dephasing. Analysis of eqs 4 and 5 indicates that decay of the dephasing function is determined by the area under the unnormalized ACF, eq 2. In turn, the area depends on the amplitude of the phonon-induced fluctuation of the electronic energy gap, which determines the initial ACF value, $C(0) = \langle \delta E^2 \rangle_T$, and the decay and asymmetry of the normalized ACF, eq 3. Larger gap fluctuation as well as longer and more asymmetric ACF favor faster dephasing. The energy gap fluctuation is largest for pristine graphane, Figure 3, and the

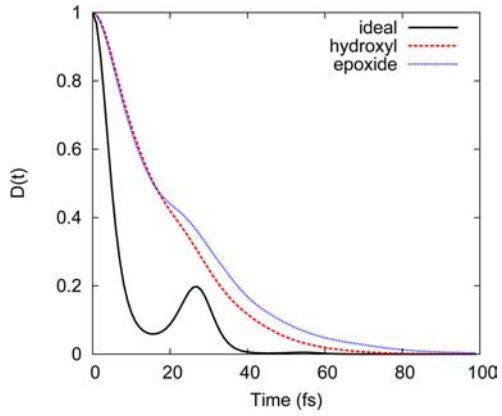

Figure 6. Dephasing functions at 300 K computed based on the ACFs, Figure 4, using the cumulant expansion, eq 4. Corresponding dephasing times reported in Table 1 were obtained by fitting the data to eq 6. Graphane oxides dephase on similar time scales, while ideal graphane exhibits much faster dephasing due to a larger fluctuation in the excitation energy, Figure 2, which determines the initial value of the unnormalized ACF, eq 2.

Table 2. Fitting Parameters, Eq 6, for Dephasing Functions, Figure 6

	A	B	τ_e (fs)	τ_g (fs)	ω (fs^{-1})
ideal	0.79	0.73	17.4	3.4	0.22
hydroxyl	0.094	0.40	18.0	19.8	0.17
epoxide	0.039	0.70	19.7	25.4	0.25

ACF decays very slowly, Figure 4. However, the ACF is very symmetrical with respect to the time axis. As a result, the integral over the unnormalized ACF encountered in eq 5 is only slightly larger for graphane than for its hydroxy and epoxy forms, leading to relatively minor differences in the dephasing times, Table 1.

Our final and main simulation result is the nonradiative decay of the lowest excited electronic state which leads to recovery of the ground-state population. In order to obtain the relaxation times, τ, reported in Table 1, we fit the 2500 fs NAMD data, Figure 7, to the expression $P(t) = 1 - \exp(t/\tau) \approx t/\tau$, assuming that the full nonradiative decay process is exponential.[36,37] Oxidation significantly accelerates relaxation, resulting in a shorter excited-state lifetime. Hydroxylation causes the greatest acceleration, reducing the relaxation time from 160 ns for ideal graphane to 4.8 ns, while epoxidation decreases the relaxation time to 13.3 ns.

Excitation energy, NA coupling, and pure dephasing are the three main factors influencing the relaxation process, Table 1. The smaller excitation energy favors faster nonradiative relaxation in hydroxylated graphane, according to the energy gap law.[75] At the same time, relaxation is also fast in epoxy graphane, even though its excitation energy is larger than in pristine graphane. The NA electron−phonon coupling

dx.doi.org/10.1021/ja400033g | J. Am. Chem. Soc. 2013, 135, 3702−3710

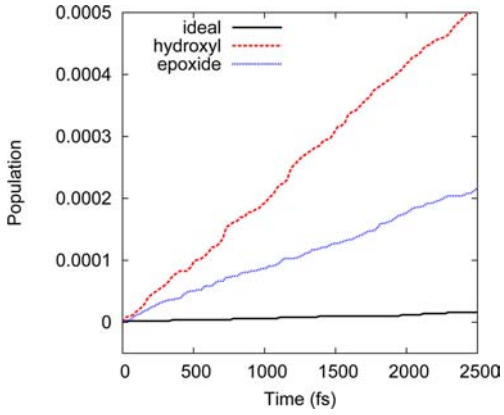

Figure 7. Ground-state population recovery due to nonradiative relaxation of the lowest energy singlet excited state at 300 K. Ideal graphane shows the lowest rate of nonradiative decay, while oxidized sheets exhibit relatively high decay rates, see Table 1.

constitutes the main factor that determines the relative values of the decay rates in the three considered systems. The electron−phonon coupling is 3−4 times larger in the oxidized forms of graphane, Table 1. Fermi's golden rule indicates that the rate depends on the square of the coupling, rationalizing the order of magnitude difference in the nonradiative excited-state lifetimes between the pristine and the oxidized graphanes. The coupling is stronger in graphane oxides, because the dipole moments of the C−O and O−H bonds interact strongly with the electronic density, while the apolar C−C bonds of pristine graphane affect the electronic density less. The interaction is strongest for the epoxide, because the photoinduced charge transfer is most pronounced in this case: the LUMO density is localized away from the graphane plane, Figure 2c. Strong electron−phonon coupling compensates for the effect of the larger excitation energy in epoxidated graphane, and as a consequence, the relaxation in both epoxide and hydroxide proceeds on similar time scales. The pure-dephasing time can be viewed as the time-domain equivalent of the Franck−Condon overlaps of vibrational wave functions associated with the two electronic states.[45] The longer pure-dephasing times of oxidized graphanes correspond to larger Franck−Condon factors and therefore larger transition rates, leading to an accelerated relaxation.

Comparing the nonradiative relaxation in graphanes on the one hand and CNTs and GNRs on the other, we find that our predicted excited-state lifetime for ideal graphane is significantly longer than those for pristine CNTs[37] and GNRs.[36] Graphane exhibits weaker NA coupling, larger excitation energy, and faster pure dephasing. All three factors contribute to slower relaxation. Graphane oxidation enhances the relaxation, similar to the defects in CNTs and GNRs.[36,37] We also observe that oxidation of graphane increases the dephasing time, similar to the defects in GNRs.[50] Phonon-induced dephasing owes its origin to cubic anharmonicity of the vibrational potential. The anharmonic vibrational potential causes a vibrational mode to have unequal preference for one side of the distorted parabolic potential, giving rise to an asymmetric and rapidly decaying ACF, Figure 4. Lack of the π-bonding network increases the flexibility of graphane compared to CNTs and GNRs, enhances anharmonicity, and favors faster pure dephasing.

The calculated electron−phonon relaxation and pure-dephasing times allow us to estimate the homogeneous spectral line widths, eq 1. The line widths can be observed in single-chromophore luminescence spectra[76] and photon-echo experiments.[77] Our calculations reveal that the pure-dephasing time, T_2^*, is on the order of femtoseconds, while the excited-state lifetime, T_1, is on the order of nanoseconds. Since the excited-state lifetime is 6 orders of magnitude larger than the pure-dephasing time, the homogeneous line widths are determined solely by the pure-dephasing times. Calculated for ambient temperature and reported in Table 1, the line widths are several tenths of meV and a factor of 2−4 larger than those obtained previously for CNTs[35] and GNRs.[50]

It is important to point out that the current simulation focused on singlet states and that the triplet-state manifold can also contribute to nonradiative relaxation of electronic excitations and ground-state recovery. One can expect, however, that the spin−orbit (SO) coupling responsible for singlet−triplet transitions is relatively small in graphanes and that it is similar to the SO coupling in graphene,[78] making intersystem crossing (ISC) unlikely to contribute significantly to the nonradiative decay. The SO coupling is much stronger in curved carbon materials, such as fullerenes and CNTs,[40,78] where ISC into triplet states constitutes an important relaxation pathway. The study is carried out using periodic DFT that employs an effective independent particle representation and incorporates the electron correlation effects into the DFT functional. More advanced many-body theories predict that the first excited state of graphane is a charge-transfer exciton.[19] The current simulation confirms the charge-transfer character of the first excited state of graphane and its oxides: the HOMO and LUMO orbitals are located in different planes, Figure 2. At the same time, the HOMO and LUMO orbitals are completely delocalized along the graphane plane, while the excitons are fairly localized.[19] In general, the electron−phonon coupling is enhanced for localized states;[35−37,50,79] therefore, one can expect that excitonic effects should speed up nonradiative quenching of luminescence and increase luminescence line width. Further, realistic systems contain edges and defects, which may affect the electron−phonon coupling and electronic energy gap. Similarly to excitons and perhaps even more significantly, the localized states formed by defects should also enhance the nonradiative relaxation and the luminescence line widths. These factors have been characterized for GNRs[36,50] and will constitute an important subject for future studies of graphanes.

4. CONCLUSIONS

By performing time-domain ab initio simulations combining NAMD and TDDFT, we demonstrated that pristine graphane should exhibit very slow nonradiative decay of the singlet excitation back to the ground state. The calculated 100 ns time scale is an order of magnitude longer in graphane than in other nanoscale carbon materials, such as CNTs, GNRs, and fullerenes. Rapid nonradiative electron−phonon relaxation limits the use of CNTs and GNRs in electronic devices but should not constitute a drawback for graphane. Slow relaxation is attributed to the weak NA electron−phonon coupling, large band gap, and rapid phonon-induced pure dephasing of the electronic excitation. The nonradiative electronic transition is promoted exclusively by the 1200 cm^{-1} phonon mode in pristine graphane. The electron−vibrational energy transfer is significantly accelerated in the oxidized forms of graphane, making the relaxation time similar to that in CNTs and GNRs. The hydroxy and epoxy functional groups introduce new types

of vibrational modes and break the strict electron−phonon coupling selection rules. As a result, a variety of phonons contribute to the nonradiative relaxation of the singlet excitation in the oxidized forms of graphane, increasing the NA coupling by a factor of 3−4 and the relaxation rate by an order of magnitude. The hydroxy and epoxy groups act as impurities, and in this regard, they are analogous to defects in CNTs and GNRs. The long lifetime of the electronic excitations in graphane ensures slow recombination of charge carriers. This property is particularly advantageous for semiconductor applications.

AUTHOR INFORMATION

Corresponding Author

E-mail: oleg.prezhdo@rochester.edu

Notes

The authors declare no competing financial interest.

ACKNOWLEDGMENTS

Financial support of grant CHE-1300118 from the National Science Foundation is gratefully acknowledged.

REFERENCES

(1) Sofo, J. O.; Chaudhari, A. S.; Barber, G. D. *Phys. Rev. B* **2007**, *75*, 153401.
(2) Elias, D. C.; Nair, R. R.; Mohiuddin, T. M. G.; Morozov, S. V.; Blake, P.; Halsall, M. P.; Ferrari, A. C.; Boukhalov, D. W.; Katsnelson, M. I.; Geim, A. K.; Novoselov, K. S. *Science* **2009**, *323*, 610.
(3) Boukhalov, D. W.; Katsnelson, M. I.; Lichtenstein, A. I. *Phys. Rev. B* **2008**, *77*, 035427.
(4) Yang, Z.; Sun, Y.; Alemany, L. B.; Narayanan, T. N.; Billups, W. E. *J. Am. Chem. Soc.* **2012**, *134*, 18689−18694.
(5) Wen, X.-D.; Yang, T.; Hoffmann, R.; Ashcroft, N. W.; Martin, R. L.; Rudin, S. P.; Zhu, J.-X. *ACS Nano* **2012**, *6*, 7142−7150.
(6) Wen, X.-D.; Hoffmann, R.; Ashcroft, N. W. *J. Am. Chem. Soc.* **2011**, *133*, 9023−9035.
(7) Talyzin, A. V.; Luzan, S.; Anoshkin, I. V.; Nasibulin, A. G.; Jiang, H.; Kauppinen, E. I.; Mikoushkin, V. M.; Shnitov, V. V.; Marchenko, D. E.; Noreus, D. *ACS Nano* **2011**, *5*, 5132−5140.
(8) Nakamura, J.; Arimura, N.; Hirayama, M.; Natori, A. *Appl. Phys. Lett.* **2009**, *94*, 223107.
(9) Li, Y.; Zhou, Z.; Shen, P.; Chen, Z. *J. Phys. Chem. C* **2009**, *113*, 15043.
(10) Flores, M. Z. S.; Autreto, P. A. S.; Legoas, S. B.; Galvao, D. S. *Nanotechnology* **2009**, *20*, 265704.
(11) Sreejith, S.; Ma, X.; Zhao, Y. *J. Am. Chem. Soc.* **2012**, *134*, 17346−17349.
(12) Chou, S. S.; De, M.; Luo, J.; Rotello, V. M.; Huang, J.; Dravid, V. P. *J. Am. Chem. Soc.* **2012**, *134*, 16725−16733.
(13) Fang, Z.; Liu, Z.; Wang, Y.; Ajayan, P. M.; Nordlander, P.; Halas, N. J. *Nano Lett.* **2012**, *12*, 3808−3813.
(14) Long, R.; English, N. J.; Prezhdo, O. V. *J. Am. Chem. Soc.* **2012**, *134*, 14238−14248.
(15) Yan, X.; Li, Q.; Li, L.-S. *J. Am. Chem. Soc.* **2012**, *134*, 16095−16098.
(16) Murray, I. P.; Lou, S. J.; Cote, L. J.; Loser, S.; Kadleck, C. J.; Xu, T.; Szarko, J. M.; Rolczynski, B. S.; Johns, J. E.; Huang, J.; Yu, L.; Chen, L. X.; Marks, T. J.; Hersam, M. C. *J. Phys. Chem. Lett.* **2011**, *2*, 3006−3012.
(17) Li, L.; Qin, R.; Li, H.; Yu, L.; Liu, Q.; Luo, G.; Gao, Z.; Lu, J. *ACS Nano* **2011**, *5*, 2601−2610.
(18) Savini, G.; Ferrari, A. C.; Giustino, F. *Phys. Rev. Lett.* **2010**, *105*, 037002.
(19) Cudazzo, P.; Attaccalite, C.; Tokatly, I. V.; Rubio, A. *Phys. Rev. Lett.* **2010**, *104*, 226804.
(20) Zhou, J.; Wang, Q.; Sun, Q.; Chen, X. S.; Kawazoe, Y.; Jena, P. *Nano Lett.* **2009**, *9*, 3867−3870.
(21) Singh, A. K.; Yakobson, B. I. *Nano Lett.* **2009**, *9*, 1540−1543.
(22) Li, Y.; Li, F.; Chen, Z. *J. Am. Chem. Soc.* **2012**, *134*, 11269−11275.
(23) Wang, Y.; Jaiswal, M.; Lin, M.; Saha, S.; Oezyilmaz, B.; Loh, K. P. *ACS Nano* **2012**, *6*, 1018−1025.
(24) Singh, A. K.; Penev, E. S.; Yakobson, B. I. *ACS Nano* **2010**, *4*, 3510−3514.
(25) Samarakoon, D. K.; Wang, X.-Q. *ACS Nano* **2009**, *3*, 4017−4022.
(26) Geim, A. K. *Science* **2009**, *324*, 1530.
(27) Li, Q.; Zhang, S.; Dai, L.; Li, L.-S. *J. Am. Chem. Soc.* **2012**, *134*, 18932−18935.
(28) Liu, L.-M.; Car, R.; Selloni, A.; Dabbs, D. M.; Aksay, I. A.; Yetter, R. A. *J. Am. Chem. Soc.* **2012**, *134*, 19011−19016.
(29) Hossain, M. Z.; Johns, J. E.; Bevan, K. H.; Karmel, H. J.; Liang, Y. T.; Yoshimoto, S.; Mukai, K.; Koitaya, T.; Yoshinobu, J.; Kawai, M.; Lear, A. M.; Kesmodel, L. L.; Tait, S. L.; Hersam, M. C. *Nat. Chem.* **2012**, *4*, 305−309.
(30) Ito, J.; Nakamura, J.; Natori, A. *J. Appl. Phys.* **2008**, *103*, 113712.
(31) Yan, J. A.; Xian, L.; Chou, M. Y. *Phys. Rev. Lett.* **2009**, *103*, 086802.
(32) Lopez-Bezanilla, A.; Triozon, F.; Roche, S. *Nano Lett.* **2009**, *9*, 2537.
(33) Lebègue, S.; Klintenberg, M.; Eriksson, O.; Katsnelson, M. I. *Phys. Rev. B* **2009**, *79*, 245117.
(34) Htoon, H.; O'Connell, M. J.; Cox, P. J.; Doorn, S. K.; Klimov, V. I. *Phys. Rev. Lett.* **2004**, *93*, 027401.
(35) Habenicht, B. F.; Kamisaka, H.; Yamashita, K.; Prezhdo, O. V. *Nano Lett.* **2007**, *7*, 3260.
(36) Habenicht, B. F.; Prezhdo, O. V. *J. Phys. Chem. C* **2009**, *113*, 14067.
(37) Habenicht, B. F.; Prezhdo, O. V. *Phys. Rev. Lett.* **2008**, *100*, 197402.
(38) Craig, C. F.; Duncan, W. R.; Prezhdo, O. V. *Phys. Rev. Lett.* **2005**, *95*, 163001.
(39) Fischer, S. A.; Habenicht, B. F.; Madrid, A. B.; Duncan, W. R.; Prezhdo, O. V. *J. Chem. Phys.* **2011**, *134*, 024102.
(40) Habenicht, B. F.; Prezhdo, O. V. *J. Am. Chem. Soc.* **2012**, *134*, 15648−15651.
(41) Runge, E.; Gross, E. K. U. *Phys. Rev. Lett.* **1984**, *52*, 997.
(42) Tully, J. C. *J. Chem. Phys.* **1990**, *93*, 1061.
(43) Parandekar, P. V.; Tully, J. C. *J. Chem. Phys.* **2005**, *122*, 094102.
(44) Jasper, A. W.; Zhu, C. Y.; Nangia, S.; Truhlar, D. G. *Faraday Discuss.* **2004**, *127*, 1−22, DOI: 10.1039/b405601a.
(45) Prezhdo, O. V.; Rossky, P. J. *J. Chem. Phys.* **1997**, *107*, 5863.
(46) Prezhdo, O. V.; Kisil, V. V. *Phys. Rev. A* **1997**, *56*, 162−175.
(47) Caro, J.; Salcedo, L. L. *Phys. Rev. A* **1999**, *60*, 842−852.
(48) Bittner, E. R.; Rossky, P. J. *J. Chem. Phys.* **1995**, *103*, 8130−8143.
(49) Mukamel, S. *Principles of Nonlinear Optical Spectroscopy*; Oxford University Press: New York, 1995.
(50) Habenicht, B. F.; Kalugin, O. N.; Prezhdo, O. V. *Nano Lett.* **2008**, *8*, 2510.
(51) Madrid, A. B.; Hyeon-Deuk, K.; Habenicht, B. F.; Prezhdo, O. V. *ACS Nano* **2009**, *3*, 2487.
(52) Stoneham, A. M. *J. Phys. D: Appl. Phys.* **1972**, *5*, 670.
(53) Home, D.; Whitaker, M. A. B. *Ann. Phys.* **1997**, *258*, 237−285.
(54) Prezhdo, O. V. *Phys. Rev. Lett.* **2000**, *85*, 4413−4417.
(55) Prezhdo, O. V.; Duncan, W. R.; Prezhdo, V. V. *Prog. Surf. Sci.* **2009**, *84*, 30−68.
(56) Casida, M. E.; Jamorski, C.; Casida, K. C.; Salahub, D. R. *J. Chem. Phys.* **1998**, *108*, 4439−4449.
(57) Long, R.; Prezhdo, O. V. *J. Am. Chem. Soc.* **2011**, *133*, 19240−19249.
(58) Fischer, S. A.; Duncan, W. R.; Prezhdo, O. V. *J. Am. Chem. Soc.* **2009**, *131*, 15483−15491.

(59) Kilina, S. V.; Kilin, D. S.; Prezhdo, O. V. *ACS Nano* **2009**, *3*, 93−99.
(60) Duncan, W. R.; Craig, C. F.; Prezhdo, O. V. *J. Am. Chem. Soc.* **2007**, *129*, 8528−8543.
(61) Duncan, W. R.; Stier, W. M.; Prezhdo, O. V. *J. Am. Chem. Soc.* **2005**, *127*, 7941−7951.
(62) Miller, W. H. *J. Chem. Phys.* **1971**, *55*, 3146.
(63) Prezhdo, O. V. *J. Chem. Phys.* **1999**, *111*, 8366−8377.
(64) Jasper, A. W.; Truhlar, D. G. *J. Chem. Phys.* **2005**, *123*, 064103.
(65) Jaeger, H. M.; Fischer, S.; Prezhdo, O. V. *J. Chem. Phys.* **2012**, *137*, 22A545.
(66) Zhu, C. Y.; Nangia, S.; Jasper, A. W.; Truhlar, D. G. *J. Chem. Phys.* **2004**, *121*, 7658−7670.
(67) Bedard-Hearn, M. J.; Larsen, R. E.; Schwartz, B. J. *J. Chem. Phys.* **2005**, *123*, 234106.
(68) Kresse, G.; Furthmüller, J. *Comput. Mater. Sci.* **1996**, *6*, 15.
(69) Perdew, J. P.; Burke, K.; Ernzerhof, M. *Phys. Rev. Lett.* **1996**, *77*, 3865.
(70) Kresse, G.; Joubert, D. *Phys. Rev. B* **1999**, *59*, 1758.
(71) Janowski, T.; Pulay, P. *J. Am. Chem. Soc.* **2012**, *134*, 17520−17525.
(72) Fokin, A. A.; Gerbig, D.; Schreiner, P. R. *J. Am. Chem. Soc.* **2011**, *133*, 20036−20039.
(73) Zhao, Y.; Truhlar, D. G. *J. Phys. Chem. C* **2008**, *112*, 4061−4067.
(74) Peelaers, H.; Hernandez-Nieves, A. D.; Leenaerts, O.; Partoens, B.; Peeters, F. M. *Appl. Phys. Lett.* **2011**, *98*, 051914.
(75) Englman, R.; Jortner, J. *Mol. Phys.* **1970**, *18*, 145−164.
(76) Pan, S. L.; Rothberg, L. J. *J. Am. Chem. Soc.* **2005**, *127*, 6087−6094.
(77) Donehue, J. E.; Varnavski, O. P.; Cemborski, R.; Iyoda, M.; Goodson, T. *J. Am. Chem. Soc.* **2011**, *133*, 4819−4828.
(78) Huertas-Hernando, D.; Guinea, F.; Brataas, A. *Phys. Rev. B* **2006**, *74*, 155426.
(79) Tretiak, S.; Kilina, S.; Piryatinski, A.; Saxena, A.; Martin, R. L.; Bishop, A. R. *Nano Lett.* **2007**, *7*, 86−92.